

Electron-Ion Recombination Rate Coefficients and Photoionization Cross Sections for Astrophysically Abundant Elements VIII. Ar XIII with new features

Sultana N. Nahar

Department of Astronomy, The Ohio State University, Columbus, OH 43210

nahar@astronomy.ohio-state.edu

ABSTRACT

Ar XIII is found to be unique with new features in electron-ion recombination not seen in any other ion. The ion has been studied with the unified method which provides a theoretically self-consistent set of atomic parameters for the inverse processes of photoionization and total electron-ion recombination. Unified method subsumes both the radiative recombination (RR) and dielectronic recombination (DR) within the framework of close-coupling formulations using the R-matrix method. A set of four DR "bumps", two in the low and two in the high temperature regions, is found to exist in the recombination rates of $\text{Ar XIV} + e \rightarrow \text{Ar XIII}$. This is in contrast to two typical DR "bumps", one at high temperature common for most ions and one at low temperature depending on the presence of near threshold autoionizing resonances in the bound-free process. Large scale ab initio calculations have been carried out for photoionization and electron-ion recombination cross sections of Ar XIII. The ion is represented by a large close coupling eigenfunction expansion of 37 core Ar XIV states from $n = 2$ and 3 complexes. This enables core excitations of type $\Delta n = 0$ and 1. The $\Delta n = 1$ transitions have much higher radiative decay rates than those of $\Delta n = 0$, and cause the fourth DR bump around 2×10^6 K. For a large number of bound states, Ar XIII exhibits more extensive resonant structures and wider PEC (photoexcitation-of-core) resonances for $n = 3$ core states than those of $n = 2$ states. Hence the high energy region of photoionization and recombination are dominated by these structures. A total of 684 bound states with valence electron $n \leq 10$ and $l \leq 9$ are found for Ar XIII. Total and partial photoionization cross sections of all bound states, state-specific recombination rates of 561 bound states and total recombination rate coefficients at a large temperature range are presented for Ar XIII.

Subject headings: Photoionization and recombination: general — State-specific and total photoionization cross sections and recombination rate coefficients: individual(ion, Ar XIII, unique features)

1. Introduction

Ar XIII has been studied less compared to many other ions and relatively little reliable atomic data are available for this ion. However, reliable atomic parameters are important to interpret the large number of high resolution spectra being taken by observatories such as HST, EUVE, FUSE, over optical to extreme ultra-violet wavelength ranges and to understand the physical conditions and properties of astrophysical and laboratory plasmas. Photoionization of Ar XIII was studied under the Opacity Project (OP, 1995, 1996) using a relatively smaller wavefunction expansion (Nahar and Pradhan 1992a). Oscillator strengths for allowed transitions including relativistic effects in Breit-Pauli R-matrix approximation were obtained by Nahar (2000). Earlier works on electron-ion recombination include radiative recombination (RR) rates by Aldrovandi and Pequignot (1974) and dielectronic recombination (DR) rates by Shull and van Steenberg (1982), Gu (2003), Altun et al. (2004).

Present work reports results of a self-consistent study of the two inverse processes photoionization and electron-ion recombination of $\text{Ar XIII} + h\nu \leftrightarrow \text{Ar XIV} + e$ employing the unified method for the total recombination. The method, in principle, provides the most accurate total recombination (RR+DR) rate coefficients with considerations of interference and channel coupling effects. Total and state specific recombination rate coefficients of other carbon like ions, e.g., from C I to S XI, were presented earlier (Nahar 1995, 1996a). However, Ar XIII appears to be a unique ion with differences to these ions. Unlike to their cores, the $n = 3$ core states of Ar XIII are separated by a large energy gap from those of $n = 2$. A smaller wavefunction expansion of 8 terms, compared to present 37 terms, was used in the earlier close coupling R-matrix calculations. Inclusion of highly excited core states in the present wavefunction expansion has revealed new features for photoionization and recombination for Ar XIII that are reported herein.

Present series of report (paper I, Nahar and Pradhan 1997) aims at studying and presenting accurate atomic parameters for photoionization and total (e+ion) recombination for astrophysical models on a variety of applications. such as planetary nebulae, active galactic nuclei, and stars. The ab initio unified treatment of Nahar and Pradhan (1992b, 1994, 1995, 2003) provides (A) total recombination rates that is valid for all temperatures, (B) level-specific recombination rates for a large number of atomic levels, and (C) self-consistent sets of photoionization cross sections, σ_{PI} , and electron-ion recombination rate coefficients,

α_R , which reduce the uncertainty in astrophysical models. In contrast, the other methods, mainly the isolated resonance approximation with distorted wave (e.g. Gu 2003, Altun et al. 2004) considers limited number of resonances, although convergence with respect to the principle quantum number could be checked for optimum contribution, and can obtain only the DR rates. The RR rates, which do not include any resonance, are calculated using distorted wave or central field or hydrogenic approximation separately to add to DR for the total.

2. Theory

The unified treatment for the total electron-ion recombination, that subsumes both the radiative and dielectronic recombination processes in an ab initio manner, enables self-consistent results for σ_{PI} and α_R by using the same wavefunction that describes the (e+ion) system for both processes, photoionization and recombination. The details of the theory are given in earlier papers (Nahar and Pradhan 1994, 1995, Nahar 1996b). A brief outline of the method is given below.

2.1. The coupled channel wavefunction expansion

In the close-coupling (CC) approximation (Seaton 1987), the 'target' or the 'core' ion is represented by an N-electron system, and while the interacting (N+1)th electron is bound or in the continuum depending on its energy. The total wavefunction, Ψ_E , of the (N+1) electron system for any symmetry $SL\pi$ is represented by an expansion of the eigenfunctions of the target ion, χ_i , coupled to the (N+1)th electron function, θ_i , as:

$$\Psi_E(e + ion) = A \sum_i \chi_i(ion)\theta_i + \sum_j c_j \Phi_j, \quad (1)$$

where the target is in a specific state $S_i L_i \pi_i$ and the (N+1)th electron is in a channel labeled $S_i L_i \pi_i k_i^2 \ell_i (SL\pi)$ where k_i^2 is its kinetic energy. The Φ_j s are bound channel functions of the (N+1)-electron system that account for short range correlation and the orthogonality between the continuum and the bound electron orbitals.

Substitution of the wavefunction expansion in

$$H_{N+1}\Psi_E = E\Psi_E. \quad (2)$$

where the (N+1)-electron Hamiltonian is,

$$H_{N+1} = \sum_{i=1}^{N+1} \left\{ -\nabla_i^2 - \frac{2Z}{r_i} + \sum_{j>i}^{N+1} \frac{2}{r_{ij}} \right\}. \quad (3)$$

introduces a set of coupled equations that are solved using the R-matrix approach (Burke et al. 1971, The Opacity Project 1995, 1996). The continuum wavefunction, Ψ_F , describes the scattering process with the free electron interacting with the target at positive energies ($E > 0$), while at negative total energies ($E \leq 0$), the solutions correspond to pure bound states Ψ_B . The complex resonant structures in photoionization and recombination result from couplings between continuum channels that are open ($k_i^2 > 0$) and bound channels that are closed ($k_i^2 < 0$) and form at electron energies k_i^2 corresponding to the Rydberg series of states converging on to the target thresholds.

2.2. Photoionization

The transition matrix elements for photoionization and recombination can be obtained using the bound and continuum wavefunctions as

$$\langle \Psi_B | \mathbf{D} | \Psi_F \rangle, \quad (4)$$

where \mathbf{D} is the dipole operator. In "length" form, $\mathbf{D}_L = \sum_i r_i$, and in "velocity" form, $\mathbf{D}_V = -2 \sum_i \Delta_i$, where the sum corresponds to number of electrons. The transition matrix element with the dipole operator can be reduced to the generalized line strength defined, in either length form as

$$S_L = | \langle \Psi_j | \mathbf{D}_L | \Psi_i \rangle |^2 = \left| \left\langle \Psi_f \left| \sum_{j=1}^{N+1} r_j \right| \Psi_i \right\rangle \right|^2, \quad (5)$$

or in velocity form as

$$S_V = E_{ij}^{-2} | \langle \Psi_j | \mathbf{D}_V | \Psi_i \rangle |^2 = \omega^{-2} \left| \left\langle \Psi_f \left| \sum_{j=1}^{N+1} \frac{\partial}{\partial r_j} \right| \Psi_i \right\rangle \right|^2. \quad (6)$$

where ω is the incident photon energy in Rydberg units, and Ψ_i and Ψ_f are the initial and final state wave functions. The photoionization cross section (σ_{PI}) is proportional to the generalized line strength (S),

$$\sigma_{PI} = \frac{4\pi^2}{3c} \frac{1}{g_i} \omega S, \quad (7)$$

where g_i is the statistical weight factor of the bound state.

2.3. Unified (e+ion) recombination

The total and state-specific recombination rate coefficients are obtained using the unified treatment within the close coupling approximation using the *same* wavefunction as for photoionization. The infinite number of recombined states of the electron-ion system are divided into two groups: (A) low- n states, $n \leq n_o$, and (B) high- n states, $n_o < n \leq \infty$, with $n_o \sim 10$.

The recombination cross sections, $\sigma_{RC}(i)$, and the recombination rate coefficients, $\alpha_R(i; T)$ of the low- n bound states of group (A) are obtained from the detailed *partial* photoionization cross sections, $\sigma_{PI}(i \rightarrow j)$, through the Milne relation (principle of detailed balance),

$$\sigma_{RC}(j) = \sigma_{PI}(i) \frac{g_i}{g_j} \frac{h^2 \omega^2}{4\pi^2 m^2 c^2 v^2}. \quad (8)$$

where g_i and g_j are the statistical weight factors of the recombining and recombined states respectively, and v is the photoelectron velocity. The recombining ion is assumed to be in the ground state.

Recombination rate coefficients of individual states are then obtained by averaging the recombination cross sections over the Maxwellian electron distribution, $f(v)$, at a given temperature as

$$\alpha_R(i; T) = \int_0^\infty v f(v) \sigma_{RC}(i, v) dv, \quad (9)$$

The sum of these individual rates $\sum_i \alpha_R(i, T)$ provides the contribution of the low- n bound states to the total recombination rate. As the cross sections include the detailed structures of autoionizing resonances, the sum corresponds to the inclusion of RR and DR in an unified and *ab initio* manner.

Recombination into the group (B) states ($n_o < n \leq \infty$) is dominated by DR via the high- n resonances converging on to the thresholds in the core ion, and the background recombination via RR is negligibly small. The theory of DR developed by Bell and Seaton (1985) is extended (Nahar and Pradhan 1994, Nahar 1996b) to compute the DR collision strengths, $\Omega(DR)$, in this energy region. Contributions come from the DR resonances belonging to excited core states that decay to the ground state via dipole allowed transitions. The recombination cross section is obtained as

$$\sigma_{RC}(DR) = \frac{\pi}{g_i k^2} \Omega(DR) a_o^2, \quad (10)$$

where k^2 is the energy of the free electron. The $\Omega(DR)$ is summed over all contributing symmetries $SL\pi$. Both the detailed and resonance averaged forms of DR collision strength

are obtained for resolution tests. The DR rate coefficients are obtained by averaging over the Maxwellian distribution function.

For consistency check on the DR calculations, independent R-matrix close coupling scattering calculation is carried out for electron impact excitation (EIE) collision strengths, $\Omega(EIE)$, at excited target thresholds using the same CC wavefunction expansion used for photoionization and recombination. As the energy from below the threshold reaches the threshold, the $\Omega(DR)$ should merge to $\Omega(EIE)$ as the captured electron via DR is released by excitation of the core.

The RR-type 'background' contributions from the high- n states, $n_o < n \leq \infty$, to the total recombination rate at all temperatures are included in the hydrogenic approximation (Nahar 1996b). These contributions are usually negligible except at very low temperatures where electron energies are not high enough for the core excitations. The low energy recombination to the infinite number of high- n states typically shows a characteristic rapid rise in α_R in the low-T region.

3. Computations

Present wavefunction expansion for Ar XIII consists of 37 lowest target terms of $n = 2$ and 3 complexes (listed in Table 1). The first 8 terms are from configurations, $2s^22p$, $2s2p^2$, and $2p^3$ of $n = 2$ complex, as used in the earlier calculations by Nahar and Pradhan (1992), and the additional 29 terms are from $n = 3$ complex. A large energy gap exists between terms of $n = 2$ and $n = 3$ complexes, the last $n = 2$ term being at 8 Ry while the first $n = 3$ term is at over 31 Ry. Such energy gap is often the criteria for cut off limit for wavefunction expansion as no new bound states are formed from these highly excited core states and the correlations due to them are usually much weaker.

The target, Ar XIV, wavefunctions are obtained from atomic structure calculations using the code SUPERSTRUCTURE (Eissner et al. 1974) that employs the scaled Thomas-Fermi-Dirac potential to generate the one-electron orbitals. The set of spectroscopic and correlation configurations, and the values of the Thomas-Fermi scaling parameter (λ_{nl}) for each orbital are given in Table 1. The table presents term energies of target Ar XIV used in the calculations. The calculated target energies have been replaced by the observed energies whenever available (term energies without the asterisks in the table). This improves the accuracy of resonance positions in the photoionization cross sections. The observed energies in Table 1 are from National Institute of Standards and Technology (NIST) database and were measured by R.L. Kelly (NIST).

The second sum in the wavefunction expansion, Eq. (1), includes all possible $(N+1)$ -electron configurations with maximum occupancies upto $2p^4$, $3s^2$, $3p^2$ and $3d^2$ for Ar XIII. All $SL\pi$ symmetries of the (e+ion) system formed from target states of the ion coupled with the interacting electron with partial waves $l \leq 9$ are included.

The R-matrix calculations were carried out using the extended version of codes developed under the Iron Project (Hummer et al. 1993, Berrington et al. 1987 and 1995, Nahar and Pradhan 1995). Calculations were carried out for two or a few symmetries at a time because of computational problems with large dimensions, memory size requirements and many CPU hours.

Spectroscopic identification of the large number of bound states was considerably challenging. The present version of the IP code for bound states, STGB, does not analyze the energy eigenvalues of the Hamiltonian for any spectroscopic identification. A computer program, PLSRAD, was written to analyze the bound states with highest the contributing channels, quantum defect numbers, to identify the Rydberg series of states and assign the spectroscopic notation. However, for closely lying states, identification may have uncertainties because of similar amount of quantum defects.

Calculations for photoionization cross sections were carried out twice, (i) for the *parital* cross sections leaving the core in the ground state and (ii) for the *total* cross sections where the core can be in its ground or excited state depending on the energy. For each state, about 15,000 points of cross sections have been calculated to resolve the resonances. Calculations of partial cross sections require much longer CPU time because of reading and writing out of the isolated contributions of channels going only to the target ground state.

The Rydberg series of autoionizing resonances in σ_{PI} are resolved in detail with an effective quantum number mesh of $\Delta\nu = 0.01$ up to $\nu = 10$. This ensures that all resonance structures upto $\nu = 10$ are resolved with a finemesh of 100 points in each interval $(\nu, \nu + 1)$. The resonances belonging to $n = 3$ thresholds, are resolved with a constant energy mesh. The resonance profiles decrease in width with effective quantum number as ν^{-3} relative to the threshold of convergence such that $\nu(E) = z/\sqrt{(E - E_t)}$ (in Ry), where E_t is the target threshold energy and E is the continuum electron energy. In the region below each target threshold, the narrow autoionizing resonances are averaged using the Gailitis resonance averaging procedure (e.g. Nahar and Pradhan 1994). The photoionization cross sections at higher photoelectron energies, beyond the highest target threshold, are extrapolated as explained in Nahar and Pradhan (1994).

The total DR cross sections in the region $n_o < \nu \leq \infty$ below each threshold are obtained for all regions with thresholds radiatively allowed to decay to the core state. STGFDR (Nahar

and Pradhan 1994) was employed to obtain $\Omega(DR)$. The transition probabilities (A -values) for dipole allowed transitions to the target ground $2s^22p(^2P^o)$ state from 2D , 2S , and 2P states of $n = 2$ and 3 complexes are obtained from the atomic structure calculations using SUPERSTRUCTURE. These A -values are given in Table 2. It may be noted that radiative decay rates for $\Delta n = 1$ are much stronger, over a magnitude higher, than those of $\Delta n = 0$ indicating strong coupling effects. This was the reason for inclusion of $n = 3$ states in the present work.

To compare the consistency of DR collision strengths, $\Omega(DR)$, electron impact excitation collision strengths, $\Omega(EIE)$, at various target thresholds are obtained in the close coupling approximation. These values are given in Table 2 alongwith the $\langle \Omega(DR) \rangle$ peak at these thresholds. Comparison shows $\Omega(DR)$ is converging to $\Omega(EIE)$. We found that such convergence is not very obvious for the high energy $n = 3$ thresholds where $\langle \Omega(DR) \rangle$ becomes much weaker, as evident from the values of $\Omega(EIE)$.

The state specific and total recombination rate coefficients were obtained using program RECOMB. The major contributions are from the photoionization cross sections and high- n DR collision strengths. Contributions from energies beyond the highest target state to infinity were obtained using the numerical technique described in Nahar and Pradhan (1994) and from the "top-up" as described in Nahar (1996b). The large amount of recombination data were processed by program PRCOMG.

4. Results and discussion

The radiative inverse processes of photoionization and electron ion recombination of Ar XIII + $h\nu \leftrightarrow$ Ar XIV + e Ar XIII are studied in detail. Features of photoionization cross sections in the low energy region of $n = 2$ core thresholds were studied earlier (Nahar and Pradhan 1992a). New features are revealed with a larger wavefunction affecting both the photoionization and recombination processes. Ar XIII is unique in showing multiple "DR" bumps in its recombination rates (Nahar 2001-02, annual report by Pinsonneault & Wing 2003).

The results were obtained twice, once using an 8-CC wavefunction expansion, as used in the previous study (Nahar and Pradhan 1992a), and then using a larger wavefunction expansion of 37 terms. The purpose was to study the effect of strong dipole transitions within the core in the high energy region.

A total of 684 bound states (N_b^T) of singlet, triplet, and quintet symmetries with $n \leq 10$ and $l \leq 9$ are obtained for Ar XIII. Large number of bound states is expected from an

element with higher charge. However, number of bound states remains the same with both 8 term and 37 term wavefunction expansions, that is. no new states are from with $n = 3$ core states. Each state is assigned with an spectroscopic identification through quantum defect analysis. As explained in the computation section, there could be mismatch or uncertainties in identification for closely lying states, especially for highly excited states, due to similar characteristics. NIST compilation table lists 28 observed states which are compared with the calculated energies in Table 3. The agreement between the calculated and observed energies is within 2% for 26 states. The largest difference is about 5% with $2s2p^23p(^1D^o)$ state.

Details of photoionization cross sections, recombination cross sections and rate coefficients are presented in separate subsections below.

4.1. Total and partial photoionization cross sections

Total photoionization cross sections (σ_{PI}) leaving the ion in various excited states are presented for all 684 bound states. However, *partial* photoionization cross sections leaving core into the ground $2s^22p(^2P^o)$ state are obtained for the 561 states of singlet and triplet symmetries. Singlets and triplets couple to the core ground state, $^2P^o$ and contribute to the total recombination rate coefficients.

Photoionization cross sections of the ground and equivalent electron states appear to be unaffected by extension of the wavefunction. However, considerable changes can be seen in the excited state photoionization cross sections. The $n=3$ core states introduce extensive resonances in the high energy region via strong coupling effects. In many cases, these resonances are considerably more prominent than those from the $n=2$ complex.

Fig. 1 presents the (a) total and (b) partial σ_{PI} for the $2s^22p^2(^3P)$ ground state of Ar XIII. The differences between total (a) and partial (b) σ_{PI} are in (i) missing some resonances and (ii) lower background at higher energies in partial σ_{PI} due to omission of contributions from channels with excited cores.

The arrows in the panels point to the photon energies at the highest core threshold for the 8 CC and for the 37CC wavefunction expansion. Much of the resonances are in the lower energy region, from ionization threshold to about 8 Ry above in both panels, and correspond to Rydberg series of autoionizing states belonging to $n=2$ core thresholds. No significant contribution come from $n=3$ core thresholds as beyond $n=2$ thresholds, the cross section decays slowly with a smooth background except for some very small and weak resonances. The resonances of $n=2$ thresholds can affect both photoionization and recombination rates in the lower temperature region. The resonance positions in the present work should be more

accurate than those by Nahar and Pradhan (1992a) since the excited threshold energies, where the resonances converge, correspond to the more accurate measured values.

Fig. 2 presents photoionization cross sections of three excited quintet states of Ar XIII, a) metastable $2s2p^3(^5S^o)$ state, and valence electron b) $2s2p^2\ ^4P3s(^5P)$, c) $2s2p^2\ ^4P4p(^5P^o)$ states. Similar to the ground state, the low energy resonances of the metastable $^5S^o$ state in panel (a) belong to $n=2$ thresholds while only some weak resonances of $n=3$ thresholds scantily fill up the background cross section. In contrast, for 5P and $^5P^o$ states the resonances due to $n=3$ thresholds at energies beyond those of $n=2$ thresholds (beyond 8 Ry from the ionization threshold), are much stronger than those of $n=2$ thresholds. The background cross section may also be enhanced considerably, such as for 5P state, at $n=3$ thresholds (at about 51.5 Ry).

At photon energies equal to that for dipole allowed transitions in the core ion, the core is excited while the outer Rydberg electron remains a ‘spectator’, weakly interacting with the core ion. This process, essentially the inverse of DR, introduces a relatively wide and pronounced resonance, known as the PEC (photo-excitation-of-core) resonance (Yu and Seaton 1987), in the photoionization cross section. Fig. 3 illustrates such PEC resonances in σ_{PI} of the Rydberg series of states, $2s^22pnf(^3F)$, with $4f \leq nf \leq 10f$, of Ar XIII. The ionization threshold for σ_{PI} moves toward lower photon energies with higher excited states. The thin set of resonances at lower energies near the ionization threshold for each state belong to $n = 2$ core states while the dense and enhanced set of resonances at higher energies belong to $n = 3$ core states. These resonances at higher energies contribute more dominantly than those of $n=2$ states to photoionization rates. The arrows in the top panel of the figure point a few PEC resonances at 2P of $n=2$, 2D , and 2P of $n=3$ thresholds, allowed for dipole transitions to the core ground state $2s^22p(^2P^o)$. PEC resonances are observed in cross sections for excited valence electron states only since they entail core excitations, and demonstrate the *departure* from near-hydrogenic behavior of cross sections of excited states.

Detailed features of *partial* photoionization cross sections for a few states, in relevance to the recombination rates, are illustrated in Fig 4. These, a) $2s^22p^2(^1D)$, b) $2p^3\ ^2P^o3d(^3D^o)$, c) $2s^22p3d(^3F^o)$ and d) $2s^22p4f(^3G)$, are among the dominant contributors to the total recombination rate coefficients of Ar XIII at various temperature regions. The equivalent electron states, such as $2s^22p^2(^1D)$ of ground configuration in panel (a), have relatively higher background cross sections that decay slowly with energies, and hence contribute considerably to $\alpha_R(T)$ for a wide range of temperature. $^3D^o$ in (b) dominant considerably at lower temperatures because of its high resonance peaks in the near threshold region. The other two states, $^3F^o$ in (c) and 3G in (d), dominant at temperatures where the resonant features are enhanced.

4.2. DR collision strengths and Recombination cross sections

The total dielectronic recombination collision strengths, $\Omega(DR)$, of highly excited group (B) states, $10 \leq n \leq \infty$, for $e + \text{Ar XIV} \rightarrow \text{Ar XIII}$ are obtained both in detailed form with resonances and in resonance averaged form. $\Omega(DR)$ in the energy regions below the excited target thresholds, 2D , 2S , and 2P of $n = 2$ complex is presented in Fig. 5 where the dotted curve represent the detailed form and the solid curve to resonance averaged one. The figure has two panels, the lower one shows the expanded and detailed structures of $\Omega(DR)$, and the upper one shows the peak values, particularly the averaged $\Omega(DR)$, as the resonances converge on to their respective thresholds. The DR features show that the density of resonances increases with effective quantum number while the background rises as ν^3 indicating an increase in electron capture via the DR process as the energy approaches the threshold. At the threshold DR drops to zero as the core ion is now excited, i.e., the trapped electron flux due to DR is released into the scattering electron-impact excitation (EIE) channels. The non-zero contributions in the figure at 2S threshold are from the next higher 2P channels.

The conservation of (photon+electron) flux requires that the peak of the resonance averaged $\Omega(DR)$ at a threshold should equal the collision strength for electron impact excitation, $\Omega(EIE)$. The filled circles in Fig. 5 are the calculated Ω_{EIE} at the thresholds and are seen to match the $\langle \Omega(DR) \rangle$ peak. The numerical values are given in Table 2 showing the good agreement. The DR contributions of high- n states below $n = 3$ core thresholds become much weaker while the contributions from lower n bound states of group (A) become important through photoionization cross sections. Table 2 shows weak core excitations for $n = 3$ thresholds.

The unified electron-ion recombination cross sections, σ_{RC} , can be obtained from sum of photorecombination cross sections of low- n bound states and DR cross sections of high- n states. Fig. 6(a) presents σ_{RC} from about zero photoelectron energy to the highest core threshold beyond which no resonant structure is expected. The low energy cross sections are dominated by Rydberg series of resonances belonging to $n = 2$ thresholds, especially up to the energy (68 eV) of $2s2p^2 \ ^2P$, the highest $n = 2$ core state accessible from the ground state via dipole transition. The peak at this threshold is mainly from DR contribution. Although the background is about zero for the rest of the energy range, the contributions are mainly from the resonant photorecombination cross sections at higher energies of Ar XIII bound states with $n \leq 10$. The high- n DR makes relatively small contribution.

The recombination rate, $\alpha_{RC} = v \times \sigma_{RC}$, at various photoelectron energies is a measurable quantity at storage rings (e.g. Savin et al. 2003). Fig. 6(b) presents the recombination rates, $\alpha_{RC}(eV)$, up to core threshold $2s2p^2 \ ^2P$. These rates should be convolved with ex-

perimental monochromatic bandwidth for direct comparison. α_{RC} for Ar XIII is dominated by the near threshold resonances. As the energy approaches to the $n = 2$ core thresholds allowed for radiative decays, DR dominates. The DR peaks are pointed by arrows at the three thresholds, $2s2p^2(^2D, ^2S, ^2P)$. Recently Savin et al. (2003) have measured such rate of a similar carbon like ion, Fe XXI, in the low energy region. Present work is expected to motivate such experiments for Ar XIII. While present results are in LS coupling, a more resolve spectrum with fine structure effects are expected to be observed in the experiment as in the case for Fe XXI.

4.3. Total and state-specific recombination rate coefficients

The total recombination rate coefficients $\alpha_R(T)$ for $(e + \text{Ar XIV}) \rightarrow \text{Ar XIII}$ are presented for over a wide range of temperatures, $1 \leq \log_{10}(T) \leq 9$, at a fine temperature mesh of $\Delta \log_{10} T = 0.1$. The numerical values are presented in Table 4.

A unique feature of multiple DR "bumps", four in total which has not been seen with any other ions, is found in the total recombination rate coefficients. These bumps enhance the total $\alpha_R(T)$ considerably, as illustrated in Fig. 7 alongwith comparison with previous calculations. The lower panel of Fig. 7 presents recombination rate coefficients for the entire temperature range and the upper two panels detail the "DR bumps". In the lower panel, the solid curve represents total unified α_R using the 37-CC expansion and the dotted curve represents the same but using the 8-CC expansion. The RR rate coefficients (dashed curve) were obtained by Aldrovandi and Pequignot (1974) using photoionization cross sections in central field for the ground state and hydrogenic approximation by Seaton (1959) for excited states. The DR rate coefficients by Shull and van Steenberg (1982) (chain dashed curve) were obtained using Burgess general formula (1965), by Gu (2003) and by Altun et al. (2004) (dot-chained) were obtained using isolated resonance approximation with distorted waves.

In the upper panels of Fig. 7, the "DR bumps" are pointed by arrows, four in the 37 CC calculations and three in the 8 CC calculations. The first two bumps at around 2000 K and 30,000 K in the total $\alpha_R(T)$ for Ar XIII are due to autoionizing resonances in the near threshold region of photoionization cross sections of states, such as $2s2p^3(^3D^o)$, $2p^33s(^3D^o)$ for the first bump and $2s2p^3(^3D^o)$, $2s^22p^2(^3P)$ for the second bump, as illustrated in Fig. 5. The second bump can be seen in the DR rates by Gu (2003) (in graphical presentation) and by Altun et al (2004). The third bump (more distinct in 8-CC rates) at high temperature at around 2.5×10^5 K is from dominance of DR near $n = 2$ core thresholds and is seen in all three previous DR calculations, by Shull and van Steenberg (1982), Gu (2003), and Altun et al. (2004). Resonances due to stronger radiative decay rates of $n = 3$ core states have

introduced another DR bump at very high temperature around 2×10^6 K, almost flattening out the third one. This bump is also seen in the DR rates of Gu (2003) and of Altun et al. (2004). Typically, the total $\alpha_R(T)$, dominated by RR at very low temperature, decreases with temperature until at high T where it rises due to the dominance of DR which is followed by a smooth decay. A low temperature "bump" in $\alpha_R(T)$ due to near threshold resonances exists for many ions, e.g. for O III (Nahar and Pradhan 1997). However, presence of four bumps has been seen only for Ar XIII so far. The new features indicate that the total rate does not necessarily have a smooth transition from RR to DR with temperature.

No DR bump is seen in the previous work by Aldrovandi and Pequignot (dashed curve) as no autoionizing resonances were included in their cross sections. However, at very low temperature their RR rate coefficient almost merges with the present rates. This is expected at very low temperature since the electrons are not energetic enough to introduce a doubly excited state for DR. The high temperature DR rates (dash-chained) by Shull and van Steenberg (1982) show fair agreement with the present results at $n = 2$ thresholds. Their rates do not show the prominent enhancement from the $n = 3$ states indicating transitions from these states were not included in the Burgess formula. Present total $\alpha_R(T)$ show very good agreement with the DR rates of Altun et al. (dot-dashed) from about 2×10^3 to 10^9 K conceding dominance of DR over RR at high temperature. However, below this temperature range, their DR rate drops down as no RR was included in their calculations.

State-specific recombination rate coefficients for individual bound states of Ar XIII are presented for 561 low- n group (A) states. (The complete set for a wide temperature range is available electronically.) These are of singlet and triplet symmetries that couple to the ground $2s^22p(^2P^o)$ state of the recombining target ion. A limited number of bound states usually dominate the total recombination rate at a given temperature. However, this number increases with increasing temperature as seen in Table 5. Table 5 lists the state-specific recombination rate coefficients of the first twenty dominant low- n bound states of group (A), in order of their percentage contributions to the total $\alpha_R(T)$, at temperatures $T = 1,000, 10,000, 100,000,$ and 1×10^6 K. The equivalent and metastable states are usually among the dominant states because of their slow decay of background photoionization cross sections. The other states dominate depending on the positions and heights of resonances in σ_{PI} , as illustrated in Fig. 5. Table 5 shows that the order and the amount of contribution of individual bound states vary with temperature. The ground state may not necessarily be the dominant contributor at all temperatures, although it is one of the important ones. Present state-specific recombination rates should be close to their effective rates at these temperatures. However, above 3×10^5 K, which corresponds to the first excited target threshold 2D for a dipole allowed transition, the state-specific rates could be underestimated some since the high- n DR contributions are not included individually. The level-resolved DR

rates of Altun et al (2004) consider limited number of resonances and do not include the RR contribution.

Present results for Ar XIII should be more accurate than the available values from previous calculations since all effects are included in an ab initio manner. Based on the very good agreement between the calculated and observed energies, with the previous electron-ion recombination calculations both at very low (Aldrovandi and Pequignot 1974) and high temperatures (Altun et al. 2004), alongwith accuracy of close coupling approximation, present rates should be accurate within 30% for the reported temperature range.

Loss of accuracy due to exclusion of radiation damping of low-n autoionizing resonances in the present work is not expected to be important. The reason is that the radiative decay rates for the dipole allowed transitions (A_{fi} in Table 2) for $n = 2$ states are several orders of magnitude lower than typical autoionization rate of $10^{13-14} \text{ sec}^{-1}$. Although radiative transition rate from $n = 3$ complex is higher, autoionization still dominates as many channels for autoionization in to the lower excited states have opened up.

Inclusion of relativistic effects may improve results some. However, fine structure will increase the number of bound levels to over a thousand (Nahar 2000). In addition, increment of core fine structure levels will require much finer energy mesh for the photoionization cross sections to resolve the narrow resonances (Zhang et al. 1999). Both Gu (2003) and Altun et al. (2004) include relativistic effects in their calculations and their results agree with the present results very well. Hence, the relativistic effects are not significant for the total recombination rates although they can be exhibited in resonant features of individual states.

5. Conclusions

Total and partial photoionization cross sections, and total and state specific recombination rate coefficients, are presented for Ar XIII using unified treatment for total electron-ion recombination within close coupling approximation and R-matrix method. Self-consistency in the atomic parameters for photoionization cross sections and recombination rates is enabled by using the same wavefunction for both the inverse processes. The large scale ab initio calculations are carried out for total photoionization cross sections of 684 bound states of Ar XIII, partial cross sections and state specific recombination rate coefficients for 651 bound states. In contrast to the general feature of the total recombination rate coefficient $\alpha_R(T)$ of smooth decay with one possible DR peak at low temperature and a typical DR bump at high temperature, Ar XIII shows a unique feature of multiple DR bumps in α_{RC} , two in the low-T and two in high-T region, not seen in any other ion.

Present results are obtained from the most detailed large scale calculations of photoionization cross sections and recombination rates for Ar XIII and should be more accurate than the existing data. Present total (RR+DR) recombination rates show very good agreement at low and high temperature with previous calculations for RR and DR rates, but represent one set of rates valid for entire range of temperature. The overall relativistic effects are not found to be important from comparison with previous relativistic distorted wave and isolated resonance calculations.

All photoionization and recombination data are available electronically from the author at: nahar@astronomy.ohio-state.edu.

This work has been partially supported by the US National Science Foundation and NASA. The computational work was carried out on the Cray SV1 at the Ohio Supercomputer Center. The atomic data for photoionization and recombination are available from the author at nahar.1@osu.edu and <http://www.astronomy.ohio-state.edu/~nahar>.

REFERENCES

- Aldrovandi, S.M.V. & Pequignot, D. 1974, *Revista Brasileira de Fisica* 4, 491
- Altun, Z., Yumak, A., Badnell, N.R., Colgun, J., Pindzola M.S., 2004, *A&A* 420, 779
- Bell, R.H. & Seaton, M.J. 1985, *J. Phys. B* 18, 1589
- Berrington, K.A., Burke, P.G., Butler, K., Seaton, M.J., Storey, P.J., Taylor, K.T., & Yan, Yu. 1987, *J. Phys. B* 20, 6379
- Berrington, K.A., Eissner, W., Norrington, P.H. 1995, *Comput. Phys. Commun.* 92, 290
- Burgess, A. 1965, *ApJ*, 141, 1588
- Burke, P.G., Hibbert, A., and Robb, W.D. 1971, *J. Phys. B* 4, 153
- Eissner, W., Jones, M., & Nussbaumer, H. 1974, *Comput. Phys. Commun.* 8, 270
- Gu, M.F., 2003, *ApJ*, 590, 1131
- Hummer, D.G., Berrington, K.A., Eissner, W., Pradhan, A.K., Saraph, H.E., & Tully, J.A. 1993, *Astron. Astrophys.* 279, 298
- Kelly, R.L. (unpublished, data available at the NIST database)

- Nahar, S.N., 1995, ApJS 101, 423
- Nahar, S.N., 1996a, ApJS 106, 213
- Nahar, S.N., 1996b, Phys. Rev. A, 53, 2417
- Nahar, S.N., 2000, Astron. Astrophys. Suppl. Ser. 127, 253
- Nahar, S.N., & Pradhan, A.K. 1992a, Phys. Rev. A, 45, 7887
- Nahar, S.N., & Pradhan, A.K. 1992b, Phys. Rev. Lett, 68, 1488
- Nahar, S.N., & Pradhan, A.K. 1994, Phys. Rev. A, 49, 1816
- Nahar, S.N., & Pradhan, A.K. 1995, ApJ, 447, 966
- Nahar, S.N., & Pradhan, A.K. 1997, ApJS 111, 339
- Nahar, S.N., & Pradhan, A.K. 2004, Special Issue on Photoeffect, Radiation Physics and Chemistry 70, 323 (Elsevier, Eds. R. H. Pratt and S. T. Manson)
- Pinsonneault, M.H. & Wing, R.F. 2003, AAS Bull. Vol. 35, No. 1, p.361
- Savin, D.W., Kahn, S.M., Gwinner, G., Grieser, M., Repnow, R., Saathoff, G., Schwalm, D., Wolf, A., Muller, A., Schippers, S., Zavodszky, P.A., Chen, M.H., Gorczyca, T.W., Zatsarinny, O., Gu, M.F., 2003, ApJS 147, 421
- Seaton, M.J. 1959, MNRAS 119, 81
- Seaton, M.J. 1987, J. Phys. B 20, 6363
- The Opacity Project*, Vol 1, 1995, Vol. 2, 1996, the Opacity Project Team, Institute of Physics Publishing
- Shull, J.M. & van Steenberg, M. 1982, ApJS 48, 95
- Yu Y. & Seaton, M.J. 1987, J. Phys. B 20, 6409
- Zhang, H.L., Nahar, S.N. & Pradhan, A.K. 1999, J. Phys. B, 32, 1459

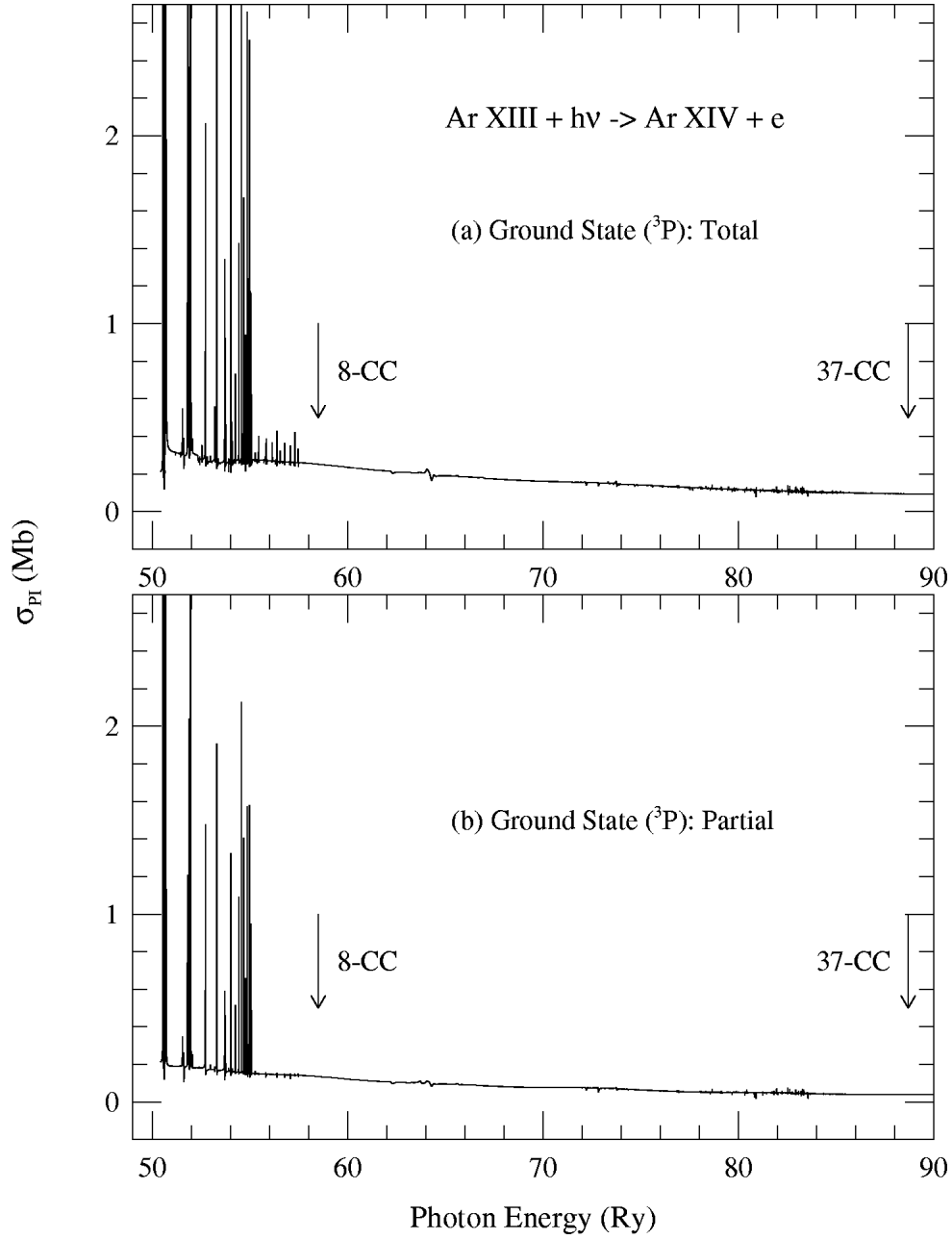


Fig. 1.— Photoionization cross sections, σ_{PI} , of the ground $2s^22p^2(^3P)$ state of Ar XIII: (a) Total - leaving the core ion in ground and various excited states, (b) Partial - leaving the core ion in the ground state. The arrows point the photon energies at the highest core threshold for the 8CC and for the 37CC wavefunction expansion. The prominent resonances in the low energy region belong to core thresholds of $n=2$ complex.

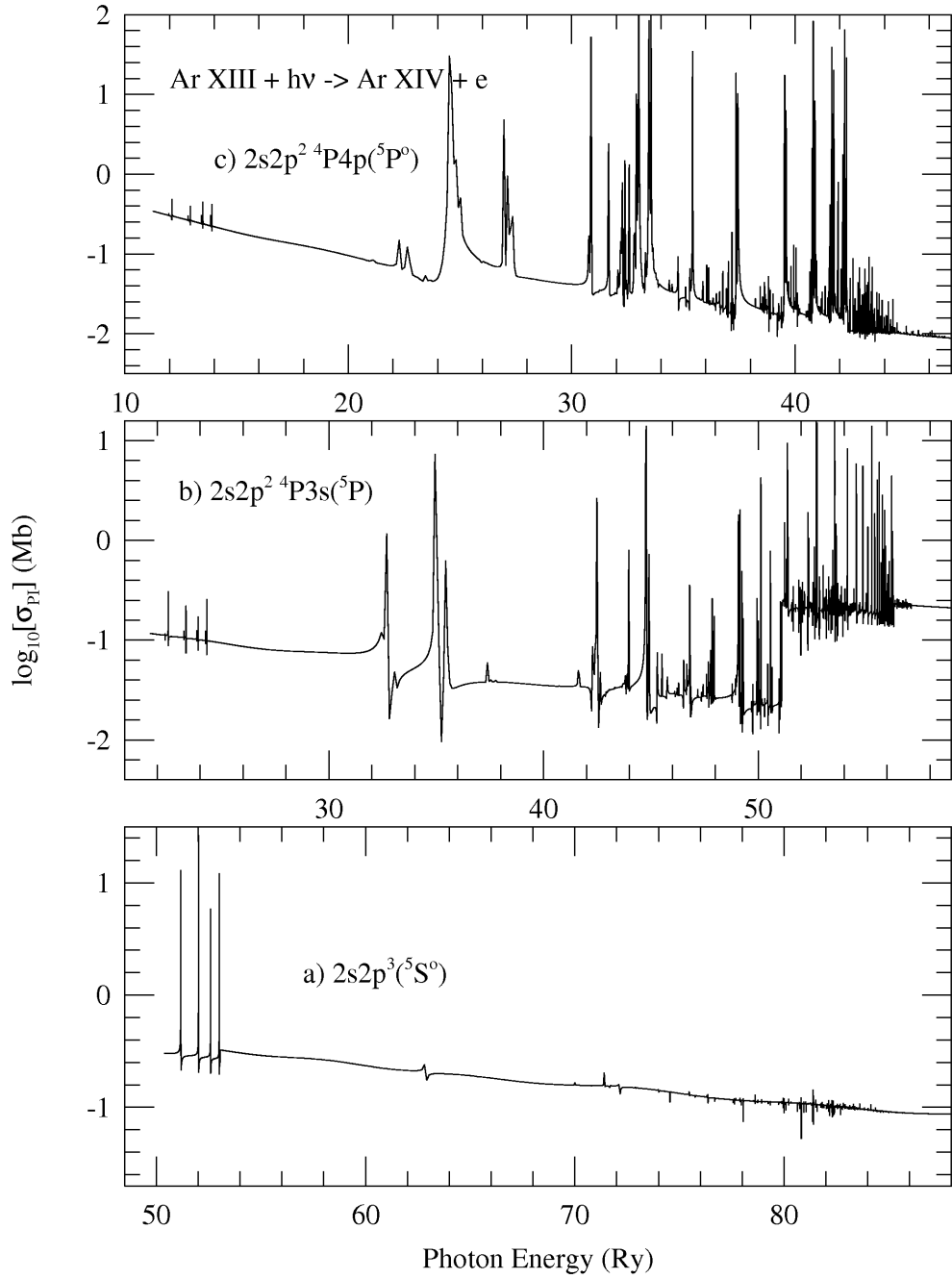


Fig. 2.— Photoionization cross sections of excited quintet states of Ar XIII illustrating coupling effects of $n=3$ core thresholds: while no significant effect is seen in σ_{PI} for the a) metastable $2s2p^3(^5S^o)$ state, extensive and much enhanced resonant features are generated for the valence electron states, b) $2s2p^2\ ^4P3s(^5P)$, and c) $2s2p^2\ ^4P4p(^5P^o)$.

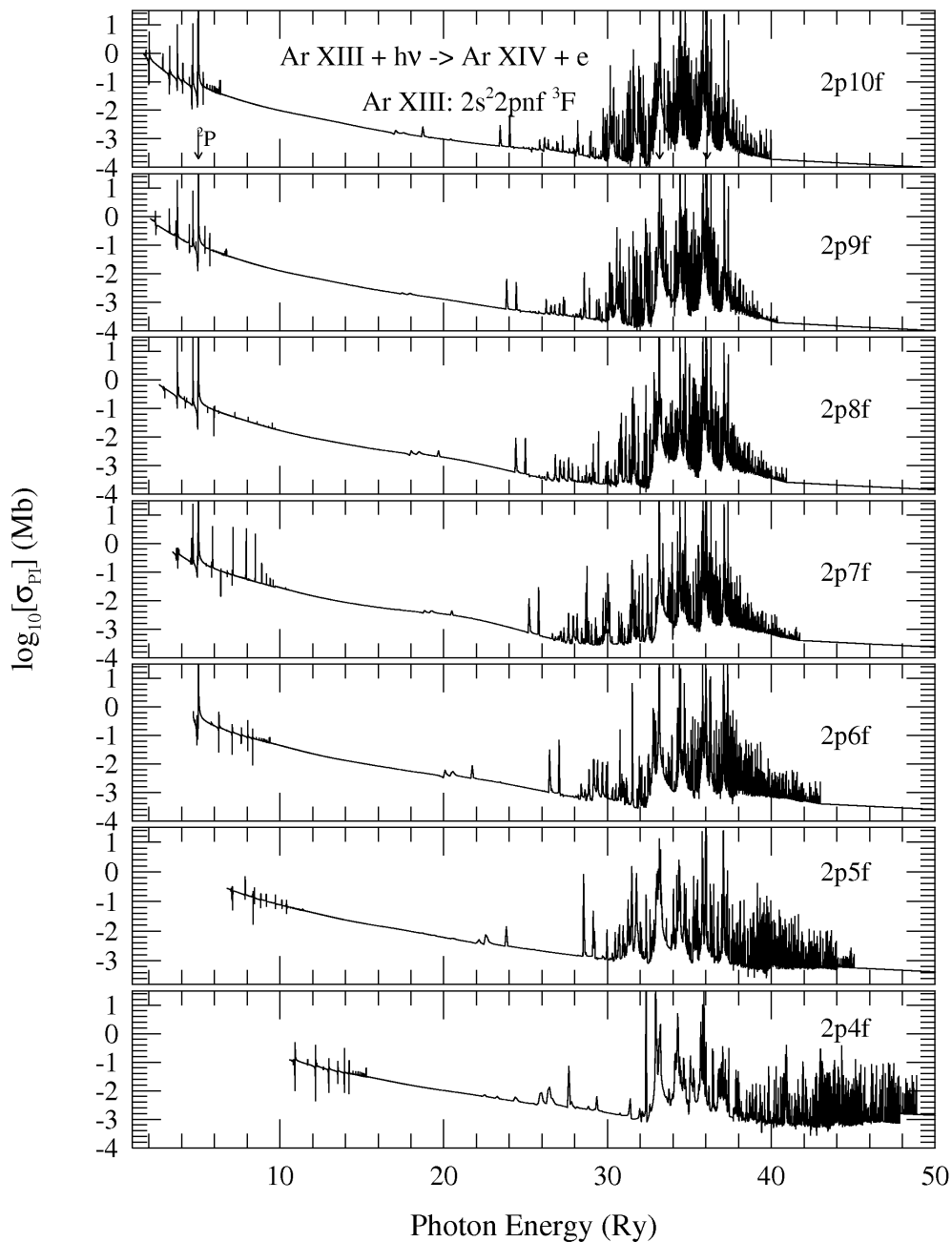


Fig. 3.— Photoionization cross sections of the Rydberg series of states, $2s^2 2pnf(^3F)$, $4f \leq nf \leq 10f$, of Ar XIII illustrating the large *photo-excitation-of-core* (PEC) resonances at high photon energies. PECs are manifested at excited core thresholds, radiatively allowed to decay to Ar XIV (core) ground state $2s^2 2p(^2P^o)$. The arrows point a few PEC positions, one at 2P state of $n=2$, and two at 2D and 2P states of $n=3$ thresholds showing much stronger PEC resonances at $n=3$ thresholds in the photon energy region of 31 - 38 Ry.

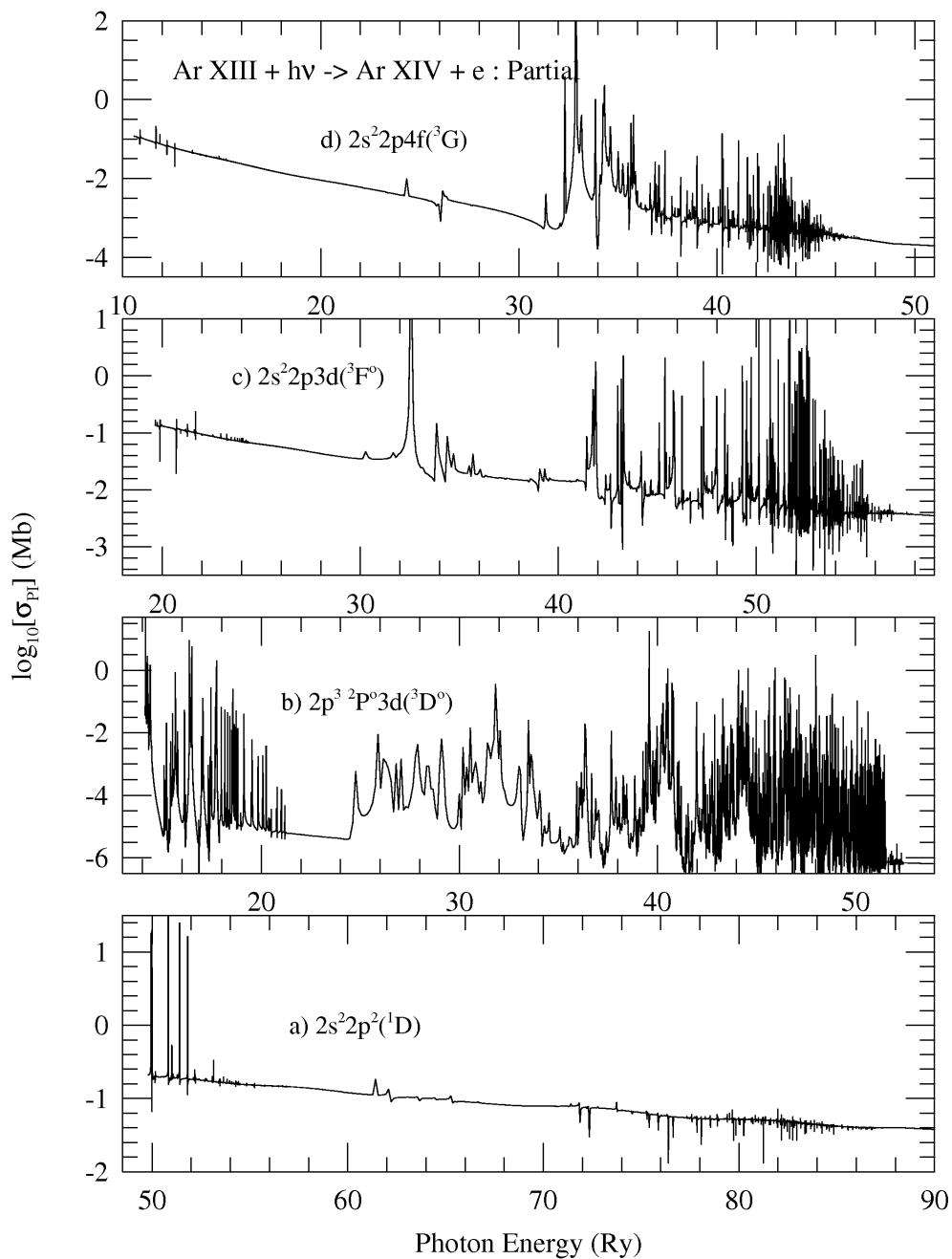


Fig. 4.— Partial photoionization cross sections of some states contributing dominantly to the total α_{RC} of Ar XIII: a) $2s^2 2p^2(^1D)$, b) $2p^3 \ ^2P^o 3d(^3D^o)$, c) $2s^2 2p 3d(^3F^o)$, d) $2s^2 2p 4f(^3G)$. The dominance is determined by the enhanced background cross sections and positions of strong resonant features.

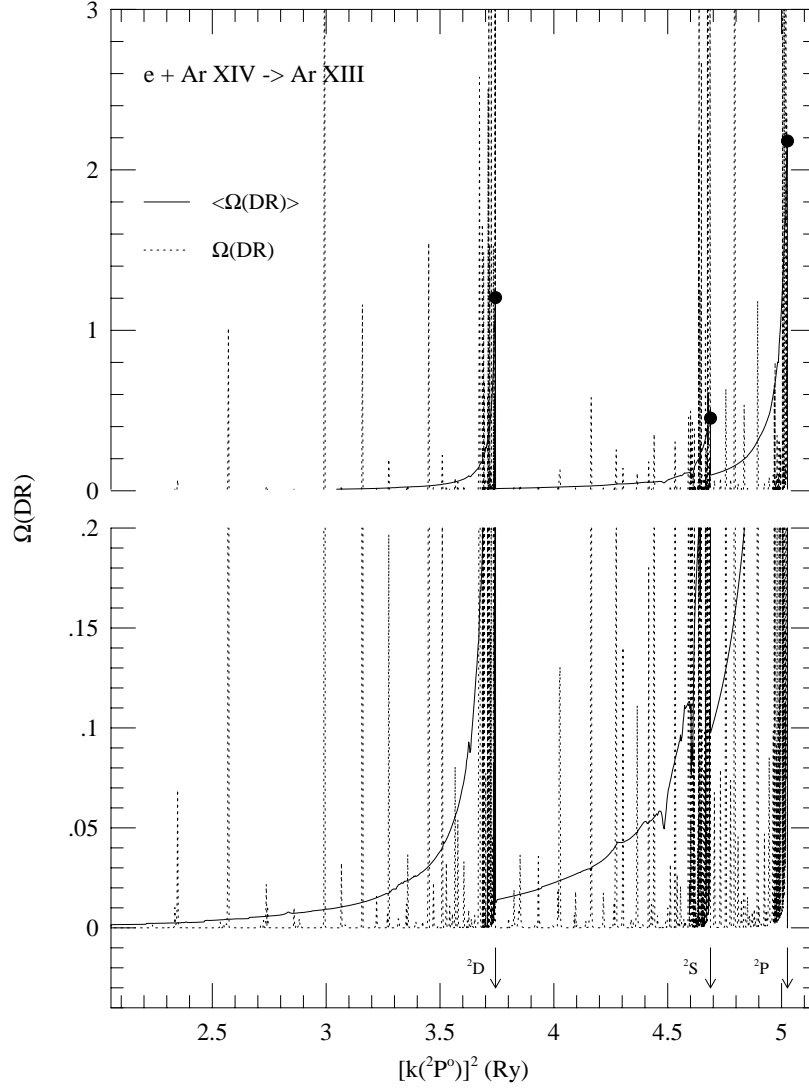


Fig. 5.— DR collision strengths $\Omega(DR)$ for Ar XIII: detailed with resonances (dotted curve), and averaged over resonances (solid curve), in the regions below and at the excited core thresholds 2D , 2S , and 2P of $n = 2$ complex (positions are specified by arrows). Lower panel shows expanded form of $\Omega(DR)$. The filled circles are the calculated electron impact excitation (EIE) collision strength, Ω_{EIE} , at the thresholds.

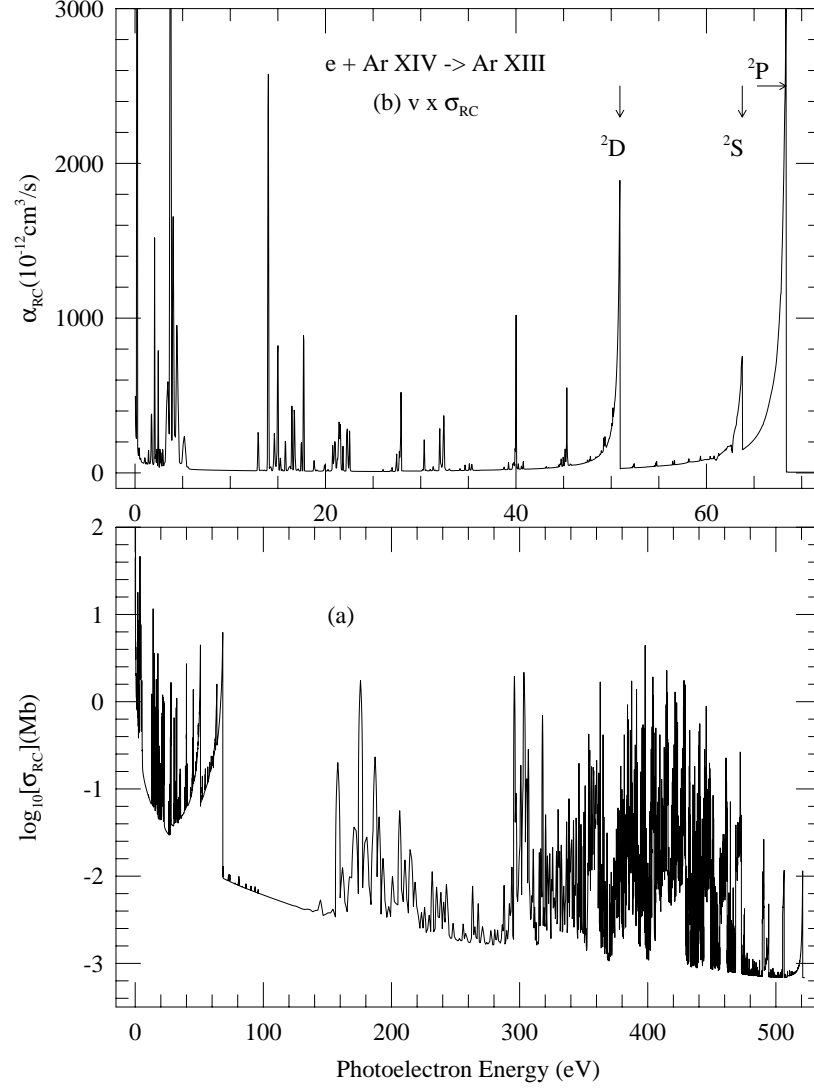


Fig. 6.— (a) The detailed unified σ_{RC} in the energy range of $n = 2$ and 3 complexes; (b) detailed recombination rate coefficient ($v \times \sigma_{RC}$) in the energy range of $n = 2$ complex. The dominant DR contributions can be seen below and at the core thresholds, 2D , 2S , and 2P .

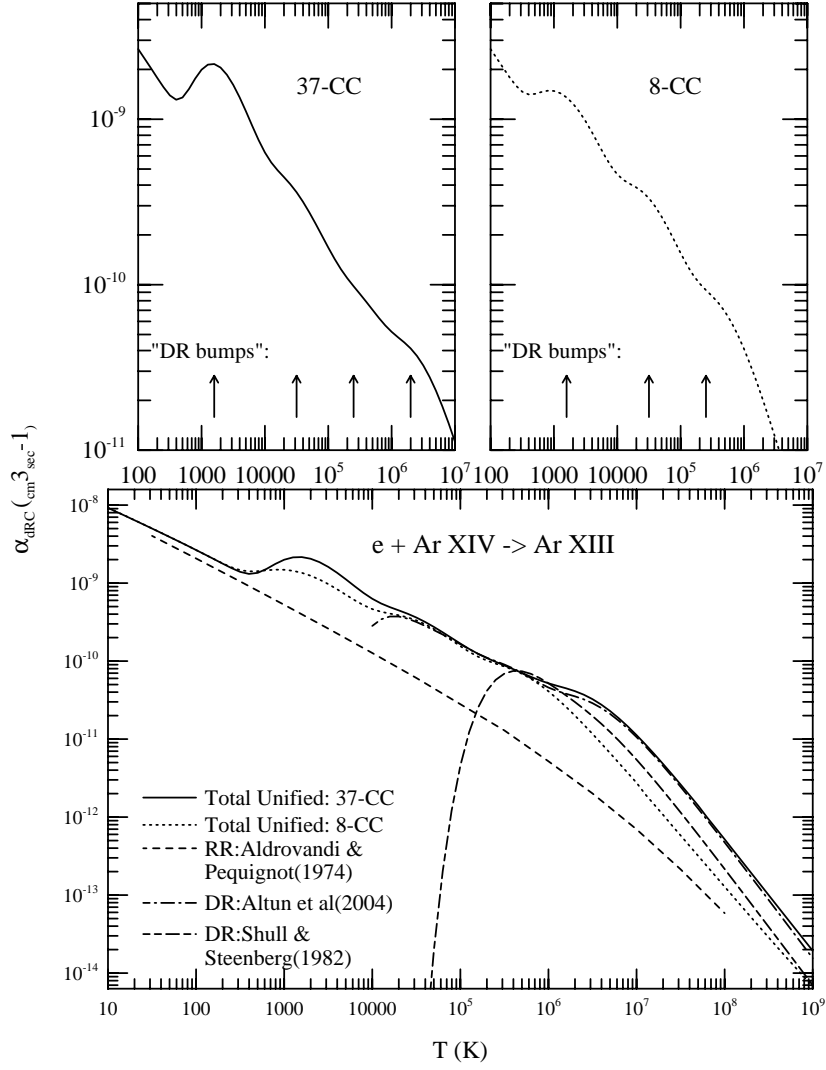


Fig. 7.— Recombination rate coefficients $\alpha_R(T)$ of $(e + \text{Ar XIV}) \rightarrow \text{Ar XIII}$. Curves in the lower panel, solid - total unified rate coefficients using the 37-CC expansion, dotted - the same but using the 8-CC expansion, dashed - RR rate coefficients of Aldrovandi and Pequignot (1974), chain-dashed - DR rate coefficients by Shull and Steenberg (1982), dot-dashed - DR rate coefficients by Altun et al. (2004). The upper two panels show the "DR bumps" (pointed by arrows), four in 37 CC calculations and three in 8 CC calculations.

Table 1. Target terms in the eigenfunction expansions of Ar XIII; an asterisk indicates that the term has not been observed. The observed energies are from NIST database measured by R.L. Kelly. $n = 2$ terms are separated from $n = 3$ terms by a large energy gap. Atomic structure calculations for the target included the spectroscopic configurations are: $2s^22p$, $2s2p^2$, $2p^3$, $2s^23s$, $2s^23p$, $2s^23d$, $2s2p3s$, $2s2p3p$, $2s2p3d$, $2p^23s$, $2p^23p$, $2p^23d$, the correlation configurations are: $2s3p^2$, $2s3d^2$, and the Thomas-Fermi scaling parameters λ_{nl} for the orbitals are: 2.4(1s), 1.37(2s), 1.45(2p), 1.4(3s), 1.15(3p), 1.1(3d).

	Term	E(Ry)		Term	E(Ry)		Term	E(Ry)
	n=2 states		12	$2s^23d(^2D)$	33.182154	25	$2s2p3p(^2P)$	35.84257
1	$2s^22p(^2P^o)$	0.0	13	$2s2p3s(^2P^o)^*$	33.53359	26	$2s2p3d(^2F^o)$	35.97162
2	$2s2p^2(^4P^e)$	1.910198	14	$2s2p3p(^4D)^*$	33.9535	27	$2s2p3p(^2P)^*$	36.03974
3	$2s2p^2(^2D^e)$	3.743752	15	$2s2p3p(^4S)^*$	34.12207	28	$2s2p3p(^2D)^*$	36.07177
4	$2s2p^2(^2S^e)$	4.687832	16	$2s2p3p(^4P)^*$	34.28115	29	$2s2p3p(^2S)^*$	36.33810
5	$2s2p^2(^2P^e)$	5.025790	17	$2s2p3p(^2D)^*$	34.44365	30	$2p^23s(^4P)^*$	36.53905
6	$2p^3(^4S^o)$	6.245461	18	$2s2p3p(^2S)^*$	34.75660	31	$2p^23s(^2P)^*$	37.13357
7	$2p^3(^2D^o)$	7.126292	19	$2s2p3d(^4F^o)^*$	34.77136	32	$2p^23p(^2S^o)^*$	37.18915
8	$2p^3(^2P^o)$	8.057424	20	$2s2p3d(^4D^o)^*$	34.98291	33	$2s2p3d(^2F^o)$	37.22526
	n=3 states		21	$2s2p3s(^2P^o)^*$	35.06681	34	$2s2p3d(^2P^o)^*$	37.22654
9	$2s^23s(^2S)$	31.56629	22	$2s2p3d(^4P^o)^*$	35.07163	35	$2p^23p(^4D^o)^*$	37.37029
10	$2s^23p(^2P^o)$	32.61456	23	$2s2p3d(^2D^o)$	35.45923	36	$2p^23s(^2D)^*$	37.38289
11	$2s2p3s(^4P^o)^*$	33.00461	24	$2s2p3d(^2P^o)^*$	35.63076	37	$2s2p3d(^2D^o)$	38.28871

Table 2: Radiative decay rates, A_{ji} , for dipole allowed transitions from various excited target states to the ground state $2s^22p(^2P^o)$, of Ar XIV; and comparison of the DR collision strength, $\langle \Omega(DR) \rangle$, with the electron impact excitation collision strength, $\Omega(EIE)$, at $n=2$ thresholds.

Target State	A_{fi} (<i>a.u.</i>)	$\Omega(EIE)$	$\langle \Omega(DR) \rangle$
$\Delta n = 0$ transitions			
$2s2p^2(^2D)$	7.46(-8)	1.204	1.272
$2s2p^2(^2S)$	3.20(-7)	0.453	0.509
$2s2p^2(^2P)$	5.86(-7)	2.180	2.162
$\Delta n = 1$ transitions			
$2s^23s(^2S)$	1.32(-5)	0.059	
$2s^23d(^2D)$	7.97(-5)	1.050	
$2s2p3p(^2D)$	3.81(-5)	0.526	
$2s2p3p(^2P)$	3.33(-5)	0.010	
$2s2p3p(^2S)$	3.84(-5)	0.019	
$2s2p3p(^2P)$	9.98(-6)	0.020	
$2s2p3p(^2D)$	2.84(-6)	0.008	
$2s2p3p(^2S)$	5.44(-6)	0.033	
$2s2p3p(^2P)$	4.15(-6)	0.003	
$2s2p3p(^2D)$	7.98(-7)	0.0009	

Table 3: Comparison of calculated energies, E_c , with measured values, E_o (kelly, NIST).

Conf	Term	$E_o(Ry)$	$E_c(Ry)$	Conf	Term	$E_o(Ry)$	$E_c(Ry)$
$2s22p2$	3P	50.191660	50.43	$2s22p3d$	$^3P^o$	19.044548	19.34
$2s22p2$	1D	49.558303	49.80	$2s22p3d$	$^1P^o$	18.740225	19.00
$2s22p2$	1S	48.855637	49.09	$2s22p3d$	$^1F^o$	18.735669	19.00
$2s2p3$	$^5S^o$	48.273847	48.49	$2s2p23p$	$^3D^o$	17.125824	16.82
$2s2p3$	$^3D^o$	46.474028	46.66	$2s2p2(4P)3d$	$^5P^*$	17.099291	17.29
$2s2p3$	$^3P^o$	45.808361	46.00	$2s2p23p$	$^1D^o$	16.019181	15.24
$2s2p3$	$^1D^o$	44.629872	44.79	$2s2p23p$	$^3P^o$	15.784439	15.87
$2s2p3$	$^3S^o$	44.603992	44.74	$2s2p23p$	$^1P^o$	15.580862	15.81
$2s2p3$	$^1P^o$	43.966379	44.13	$2s2p23p$	$^3S^o$	15.563001	15.54
$2s22p3s$	$^3P^o$	21.597007	21.88	$2s22p4s$	$^1P^o$	11.826441	11.68
$2s22p3s$	$^1P^o$	21.381077	21.69	$2s22p4s$	$^3P^o$	11.579852	11.63
$2s22p3d$	$^3F^o$	19.385940	19.64	$2s22p4d$	$^1P^o$	10.773927	10.66
$2s22p3d$	$^1D^o$	19.398160	19.65	$2s22p4d$	$^1D^o$	10.598964	10.84
$2s22p3d$	$^3D^o$	19.164663	19.40	$2s22p4d$	$^3P^o$	10.564700	10.78

Table 4: Total recombination rate coefficients, $\alpha_R(T)$ in cm^3sec^{-1} , for $e + \text{Ar XIV} \rightarrow \text{Ar X III}$ in temperature range, $1 \leq \log_{10}T(K) \leq 9$.

$\log_{10}T(K)$	α_R	$\log_{10}T$	α_R	$\log_{10}T$	α_R
1.0	9.20E-09	3.7	1.12E-09	6.4	3.71E-11
1.1	8.16E-09	3.8	9.12E-10	6.5	3.25E-11
1.2	7.23E-09	3.9	7.49E-10	6.6	2.77E-11
1.3	6.40E-09	4.0	6.30E-10	6.7	2.29E-11
1.4	5.66E-09	4.1	5.48E-10	6.8	1.84E-11
1.5	5.01E-09	4.2	4.92E-10	6.9	1.45E-11
1.6	4.42E-09	4.3	4.47E-10	7.0	1.12E-11
1.7	3.90E-09	4.4	4.05E-10	7.1	8.57E-12
1.8	3.43E-09	4.5	3.62E-10	7.2	6.46E-12
1.9	3.02E-09	4.6	3.17E-10	7.3	4.81E-12
2.0	2.65E-09	4.7	2.74E-10	7.4	3.56E-12
2.1	2.33E-09	4.8	2.34E-10	7.5	2.62E-12
2.2	2.04E-09	4.9	1.98E-10	7.6	1.92E-12
2.3	1.78E-09	5.0	1.68E-10	7.7	1.40E-12
2.4	1.56E-09	5.1	1.43E-10	7.8	9.93E-13
2.5	1.39E-09	5.2	1.24E-10	7.9	7.19E-13
2.6	1.31E-09	5.3	1.09E-10	8.0	5.19E-13
2.7	1.35E-09	5.4	9.79E-11	8.1	3.73E-13
2.8	1.52E-09	5.5	8.79E-11	8.2	2.68E-13
2.9	1.76E-09	5.6	7.88E-11	8.3	1.93E-13
3.0	1.99E-09	5.7	7.04E-11	8.4	1.39E-13
3.1	2.14E-09	5.8	6.29E-11	8.5	9.98E-14
3.2	2.16E-09	5.9	5.67E-11	8.6	7.18E-14
3.3	2.05E-09	6.0	5.19E-11	8.7	5.17E-14
3.4	1.86E-09	6.1	4.81E-11	8.8	3.72E-14
3.5	1.61E-09	6.2	4.48E-11	8.9	2.68E-14
3.6	1.36E-09	6.3	4.12E-11	9.0	1.93E-14

Table 5. State-specific recombination rate coefficients (in units of $cm^3 sec^{-1}$) of the 20 dominant states of Ar XIII at temperatures $T = 1 \times 10^3, 1 \times 10^4, 1 \times 10^5$ and 1×10^6 K in order of their contributions to the total $\alpha_R(T)$.

State	α_R	State	α_R	State	α_R	State	α_R
T(K)= 1,000		10,000		100,000		1000,000	
$2s2p^3 \ ^3D^o$	9.17-10	$2s2p^3 \ ^3D^o$	2.76-10	$2s^22p^2 \ ^3P^e$	1.93-11	$2s^22p^2 P^o3d \ ^3D^o$	3.87-12
$2p^3 \ ^2D^o3s \ ^3D^o$	1.88-10	$2p^3 \ ^2D^o3s \ ^3D^o$	5.63-11	$2s2p^3 \ ^3D^o$	1.46-11	$2s^22p^2 P^o3d \ ^3F^o$	2.11-12
$2p^3 \ ^2D^o4s \ ^3D^o$	6.64-11	$2s^22p^2 \ ^3P^e$	2.53-11	$2s^22p^2 \ ^1D^e$	1.00-11	$2s^22p^2 \ ^3P^e$	1.73-12
$2s^22p^2 \ ^3P^e$	3.38-11	$2p^3 \ ^2D^o4s \ ^3D^o$	1.99-11	$2s^22p^2 P^o4p \ ^3P^e$	4.92-12	$2s^22p^2 \ ^1D^e$	1.51-12
$2p^3 \ ^2D^o4d \ ^3F^o$	2.83-11	$2s^22p^2 \ ^1D^e$	1.06-11	$2p^3 \ ^2D^o3d \ ^3G^o$	4.02-12	$2s^22p^2 P^o4f \ ^3G^e$	8.49-13
$2p^3 \ ^2D^o4d \ ^3D^o$	2.67-11	$2p^3 \ ^2D^o4d \ ^3F^o$	8.57-12	$2s2p^3 \ ^3S^o$	3.98-12	$2s2p^3 \ ^3D^o$	7.20-13
$2s^2p^2 \ ^2D^e5p \ ^3D^o$	2.07-11	$2p^3 \ ^2D^o4d \ ^3D^o$	7.93-12	$2s2p^3 \ ^3P^o$	3.08-12	$2s^22p^2 P^o3p \ ^1P^e$	6.78-13
$2s^22p^2 \ ^1D^e$	1.78-11	$2s2p^2 \ ^2D^e5p \ ^3D^o$	6.21-12	$2s2p^2 \ ^2D^e3d \ ^3P^e$	2.55-12	$2s^22p^2 P^o4p \ ^3D^e$	6.43-13
$2p^3 \ ^2D^o3d \ ^3F^o$	1.69-11	$2p^3 \ ^2D^o3d \ ^3F^o$	5.42-12	$2s^22p^2 \ ^1D^e$	2.44-12	$2s^22p^2 P^o3p \ ^3D^e$	6.25-13
$2s2p^2 \ ^2S^e4f \ ^3F^o$	1.61-11	$2p^3 \ ^2D^o3d \ ^3D^o$	4.49-12	$2p^3 \ ^2D^o3s \ ^3D^o$	2.35-12	$2s2p^2 \ ^4P^e3d \ ^3D^e$	6.15-13
$2p^3 \ ^2D^o3d \ ^3D^o$	1.52-11	$2s^22p^2 P^o4p \ ^3P^e$	4.09-12	$2p^3 \ ^2D^o4d \ ^3G^o$	2.27-12	$2s2p^3 \ ^3P^o$	3.25-13
$2s2p^2 \ ^2P^e3p \ ^3D^o$	8.93-12	$2s2p^2 \ ^2P^e3s \ ^1P^e$	3.91-12	$2s^22p^2 P^o7i \ ^3I^o$	2.23-12	$2s^22p^2 P^o4p \ ^3P^e$	3.23-13
$2s^22p^2 P^o9g \ ^3F^o$	8.43-12	$2s2p^2 \ ^2P^e3p \ ^3D^o$	3.06-12	$2s2p^3 \ ^1D^o$	2.17-12	$2s^22p^2 P^o3p \ ^1D^e$	2.93-13
$2s2p^2 \ ^2S^e5g \ ^3G^e$	7.80-12	$2s2p^3 \ ^1D^o$	2.99-12	$2s^22p^2 P^o3p \ ^3P^e$	1.96-12	$2s^22p^2 P^o4d \ ^3F^o$	2.89-13
$2s^22p^2 P^o3d \ ^3F^o$	7.70-12	$2s2p^3 \ ^3P^o$	2.80-12	$2s^22p^2 P^o7i \ ^3K^o$	1.92-12	$2s^22p^2 P^o4f \ ^3F^e$	2.74-13
$2s^22p^2 P^o3p \ ^3D^e$	7.12-12	$2s2p^3 \ ^3S^o$	2.61-12	$2s^22p^2 P^o7i \ ^3H^o$	1.87-12	$2s^22p^2 \ ^1D^e$	2.72-13
$2s2p^2 \ ^2D^e5p \ ^3F^o$	6.96-12	$2s2p^2 \ ^2D^e3p \ ^3F^o$	2.54-12	$2p^3 \ ^2D^o3d \ ^3F^o$	1.49-12	$2s2p^2 \ ^2D^e3s \ ^1D^e$	2.45-13
$2s2p^2 \ ^2S^e3d \ ^3D^e$	6.63-12	$2s^22p^2 P^o3d \ ^3F^o$	2.41-12	$2s2p^2 \ ^2P^e3d \ ^3F^e$	1.41-12	$2s^22p^2 P^o3p \ ^3P^e$	2.38-13
$2s2p^2 \ ^2D^e3p \ ^3F^o$	6.31-12	$2s^22p^2 P^o3p \ ^3P^e$	2.31-12	$2s2p^2 \ ^2D^e3s \ ^1D^e$	1.22-12	$2s2p^3 \ ^3S^o$	2.25-13
$2s^22p^2 P^o4p \ ^3P^e$	5.61-12	$2s2p^2 \ ^2D^e5p \ ^3F^o$	2.29-12	$2s2p^3 \ ^1P^o$	1.14-12	$2p^3 \ ^2D^o3d \ ^3G^o$	2.02-13
Sum=	1.41-09		4.50-10		8.49-11		1.60-11
Total=	1.99-09		6.30-10		1.68-10		5.19-11
%contribution=	71%		72%		51%		31%